Determination of molecular gas properties using methyl cyanide lines

S.V. Kalenskii[1], V.G. Promislov[1], A.V. Alakoz[1], A. Winnberg[2], and L.E.B. Johansson[2]

[1] Astro Space Center of Lebedev Physical Institute, Profsoyuznaya 84/32, 117810 Moscow, Russia
email: kalensky@dpc.asc.rssi.ru, vitaly@diogen.asc.rssi.ru, alakoz@dpc.asc.rssi.ru

[2] Onsala Space Observatory, S-439 92, Onsala, Sweden
e-mail: anders@oso.chalmers.se, leb@oso.chalmers.se

October 22, 1999

Abstract

A survey of 27 galactic star-forming regions in the 6_K-5_K, 5_K-4_K, and 8_K-7_K CH_3CN lines at 110, 92, and 147 GHz, respectively, was made. Twenty-five sources were detected at 110 GHz, nineteen at 92 GHz, and three at 147 GHz. The strongest CH_3CN emission arise in hot cores in the regions of massive star formation. CH_3CN abundance in these objects is larger than 10^{-9} due to grain mantle evaporation. Weaker CH_3CN lines were found in a number of sources. They may arise either in warm (30-50 K) dense (10^5–10^7 cm^{-3}) clouds, or in hot regions accompanied by colder gas.

Key words: ISM: clouds – ISM: molecules – Radio lines: ISM

1. Introduction

Methyl cyanide (CH_3CN) radio emission was first detected in space by Solomon et al. (1971). Like other symmetric top molecules, e.g., ammonia or methyl acetylene, methyl cyanide is a good temperature probe for interstellar gas. Since radiative transitions between different K-ladders are prohibited in symmetric tops, the population of different K-ladders is determined by collisions and relative intensities of lines with different quantum numbers K are strongly related to kinetic temperature. CH_3CN has a large number of rotational transitions, which are grouped in series of closely spaced lines with the same J but different K quantum numbers. These lines can be observed simultaneously with the same receiver and spectrometer. Therefore the kinetic temperature estimates are not affected by calibration and pointing errors (Hollis et al. 1981; Loren & Mundy 1984). The CH_3CN spectral characteristics are well known (see e.g. Boucher et al. 1980; Loren & Mundy 1984).

With its high dipole moment (3.91 debyes) CH_3CN is a tracer of dense gas. It is well known that the CH_3CN radio emission often arises in hot gas, in particular in hot cores, i.e. hot and dense neutral regions with sizes a few 0.01 pc. Interferometric observations of several strong CH_3CN sources show that the hot core emission in their spectra is dominant, but sometimes is accompanied by a much weaker halo emission (see, e.g., Olmi et al. 1996, and references therein). The reason for strong CH_3CN emission in hot cores is grain mantle evaporation, which leads to a significant increase of CH_3CN abundance. This may occur either due to CH_3CN evaporation or due to a chain of gas-phase reactions, starting from HCN or some other nitrogen-bearing molecule, which appears in gas phase due to mantle evaporation (Millar 1996). Besides hot cores, CH_3CN has been detected toward warm clouds (30–50 K) in regions of massive star formation (Olmi et al. 1993) and in dark clouds (Irvine et al. 1987). In spite of a relatively large number of interferometric observations of hot cores in various CH_3CN lines, only a few CH_3CN surveys have been published, each of them devoted only to a small number of objects (Bergman & Hjalmarson 1989; Churchwell et al. 1992; Olmi et al. 1993). Therefore, following our previous studies of molecular clouds in various methanol lines (Kalenskii et al. 1997; Slysh et al. 1999), we made a more extended survey of Galactic star-forming regions in the 6_K-5_K and 5_K-4_K series of methyl cyanide lines near 110 and 92 GHz, respectively. Three sources were additionally observed in the 8_K-7_K lines near 147 GHz.

2. Observations

The observations at 92 and 110 GHz were carried out in April–May 1996 using the 20-m millimetre-wave telescope of the Onsala Space Observatory. The pointing accuracy was checked by observations of SiO masers and was found to be within 5″. Main beam efficiency and half-power beamwidth at 92 GHz were 0.55 and 39″, respectively. The observations were performed in a dual-beam switching mode with a switch frequency of 2 Hz and a beam separation of 11′. In no case we detected absorption features indicating that the OFF beam crossed another source component. A cryogenically cooled low-noise SIS mixer was used at both frequencies. The single sideband receiver noise temperature was about 150 K. The system noise temperature, corrected for atmospheric

Table 1: Frequencies and line strengths of the CH_3CN transitions

Transition	Frequency[1] (MHz)	Line strength
$5_0 - 4_0$	91987.090	5.00
$5_1 - 4_1$	91985.317	4.80
$5_2 - 4_2$	91980.089	4.20
$5_3 - 4_3$	91971.310	3.20
$5_4 - 4_4$	91959.024	1.80
$6_0 - 5_0$	110383.522	6.00
$6_1 - 5_1$	110381.404	5.83
$6_2 - 5_2$	110375.052	5.33
$6_3 - 5_3$	110364.469	4.50
$6_4 - 5_4$	110349.659	3.33
$6_5 - 5_5$	110330.627	1.83
$8_0 - 7_0$	147174.592	8.00
$8_1 - 7_1$	147171.756	7.88
$8_2 - 7_2$	147163.248	7.50
$8_3 - 7_3$	147149.073	6.88
$8_4 - 7_4$	147129.236	6.00
$8_5 - 7_5$	147103.744	4.87

[1]–from the database by Lovas (http://physics.nist.gov/)

absorption, rearward spillover and radome losses, varied at both frequencies between 350 and 2000 K, depending on the weather conditions and source elevation. The data were calibrated using the standard chopper-wheel method. The backend consisted of two parallel filter spectrometers: a 256-channel spectrometer with 250 kHz frequency resolution and a 512-channel spectrometer with 1 MHz frequency resolution. Two objects, NGC 1333 IRAS2 and L 1157, were observed only with the 1 MHz resolution.

The observations at 147 GHz were carried out on October 4, 1998 using the 12-m telescope NRAO[1] at Kitt-Peak, AZ, in a remote-observing mode from the Astro Space Center, Moscow. The observations were performed in a position switching mode with a position separation of $5'$. A cooled SIS-mixer, dual polarization channel receiver was used. Both senses of polarization were observed simultaneously. The data were calibrated using the standard vane method. The system noise temperature, corrected for atmospheric absorption, rearward spillover and ohmic losses, varied between 300 and 500 K. The pointing accuracy was found to be within $5''$. Main beam efficiency and half-power beamwidth were 0.54 and $42''$, respectively. The backend consisted of two 512-channel filter bank spectrometers with 1 MHz frequency resolution, connected to different polarization channels.

The frequencies and strengths of the observed CH_3CN lines are presented in Table 1.

At 110 GHz 27 sources were observed. Of those 19 were observed at 92 GHz and 3 at 147 GHz. Spectra were reduced using the Grenoble CLASS package. We made Gaussian fitting assuming that different K-components in each series have common LSR velocities and linewidths. The results are presented in Table 2.

Five objects, Ori S6, G30.8-0.1, G34.26+0.15, W 51E1/E2 and DR 21(OH) were mapped at 110 GHz. We made maps of the integrated intensity over the velocity range occupied by the blend of the 6_0-5_0 and 6_1-5_1 lines. The mapping was performed during excellent weather conditions with the system noise temperature about 350 K. The images were reconstructed using the maximum entropy (ME) technique. The method used is similar to that described by Wilczek & Drapatz (1985) except the computational algorithm to solve the optimization problem. The evolutionary algorithm, used here, is described in Promislov (1999). We estimated the effective HPBW of the reconstruction in a manner, similar to that used by Moriarty-Schieven et al. (1987). For each point of a map we subtracted the contribution from the source leaving us with the noise fluctuations only. Then for each point we added the contribution from a "test" point source, located at the position of ME map brightness peak, convolved with the beam, and had flux equal to that of the real source. We applied the ME procedure to the maps produced in this manner and obtained the brightness distribution, the FWHP of which was adopted as the effective HPBW of the reconstruction.

3. Results

Emission at 110 GHz was detected towards 25 objects of the 27 observed (S 252, W 48 and DR 21 West were only marginally detected). Sixteen objects were found at 92 GHz and 3 at 147 GHz. The spectra are presented in Figs. 1, 2, and 3, respectively. The source coordinates and the gaussian parameters of the detected lines are given in Table 2.

The ME images are shown in Fig. 4. Due to a number of reasons (mainly, relatively large telescope beam and not sufficient sampling and sensitivity) we could not resolve the sources even with the ME technique. On our maps the FWHP of the image of each source proved to be very close to the corresponding effective HPBW of the reconstruction. Thus, the results of the mapping are consistent with compact source structures, supporting the indirect size estimates, given in Table 4.

Besides the main CH_3CN isotopomer lines, a weak blend of the 5_0-4_0 and 5_1-4_1 $CH_3^{13}CN$ lines at 91941.596 and 91939.834 MHz, respectively, was detected towards G34.26+0.15. The integrated intensities of the $K = 0$ and $K = 1$ lines are 0.27 and 0.31 K km s^{-1}. The ratios of the $CH_3^{13}CN/CH_3^{12}CN$ line intensities, about 0.15, are much higher than the abundance of ^{13}C relative to ^{12}C, strongly suggesting that the CH_3CN lines are optically thick. This assumption was confirmed by rotational diagrams and statistical equilibrium (SE) calculations (see below). Similar

[1]NRAO is operated by Associated Universities, Inc., under contract with the National Science Foundation

Table 2: Gaussian parameters of the detected CH_3CN lines with their 1σ errors. For each source the parameters of the 110 GHz lines are given in the first row and those of the 92 GHz lines in the second row. For Ori S6, W 75N$(0'', 0'')$, and NGC 7538S the parameters of the 147 GHz lines are given in the third rows.

Source	R.A.$_{B1950.0}$	$\int T_A^* dV$ (K km s^{-1})						V_{LSR}	ΔV
	DEC.$_{B1950.0}$	$K=0$	$K=1$	$K=2$	$K=3$	$K=4$	$K=5$	(km s^{-1})	(km s^{-1})
W 3(OH)	02 23 17.3	0.97(0.06)	1.06(0.06)	0.80(0.01)	0.79(0.04)	0.24(0.04)	<0.12	−47.5(0.2)	8.4(0.2)
	61 38 58	0.61(0.05)	0.47(0.05)	0.29(0.04)	0.27(0.04)	< 0.09		−47.5(0.2)	6.9(0.3)
NGC 1333	03 25 55.0	<0.18							
	31 04 00	not observed							
Ori S6	05 32 44.8	2.12(0.08)	2.00(0.08)	1.03(0.07)	0.83(0.07)	<0.21		6.9(0.1)	4.2(0.1)
	−05 26 00	0.97(0.07)	0.86(0.07)	0.53(0.07)	0.31(0.07)	<0.3		6.8(0.2)	4.7(0.2)
		0.77(0.07)	0.68(0.07)	0.36(0.07)	0.48(0.07)	<0.21		6.7(0.2)	4.4(0.2)
OMC 2	05 32 59.9	0.35(0.06)	0.44(0.07)	<0.18				11.2(0.1)	2.1(0.2)
	−05 11 29	< 0.11							
S 231	05 35 51.3	0.33(0.04)	0.31(0.04)	0.18(0.04)	0.23(0.04)	< 0.12		-15.9(0.2)	3.0(0.0)
	35 44 16	0.27(0.06)	0.28(0.07)	0.14(0.07)	< 0.09			−15.6(0.4)	3.8(0.5)
S 235	05 37 31.8	0.31(0.06)	0.26(0.05)	0.22(0.05)	<0.15			−17.1(0.6)	4.7(0.4)
	35 40 18	0.22(0.04)	< 0.1					−17.1(0.0)	3.7(0.0)
S 252	06 05 53.7	0.24(0.08)[1]	0.18(0.08)[1]	< 0.24				2.9(0.9)	5.0(0.0)
	21 39 09	<0.09							
S 269	06 11 46.5	<0.06							
	13 50 39.0	not observed							
NGC 2264	06 38 24.9	0.49(0.04)	0.41(0.04)	0.22(0.04)	0.17(0.04)	<0.12		8.5(0.2)	4.0(0.2)
IRS1	09 32 28	0.34(0.07)	0.26(0.07)	< 0.2				7.8(0.5)	4.0(0.0)
G29.95-0.02	18 43 27.1	0.53(0.09)	0.73(0.09)	0.51(0.10)	0.39(0.09)	0.39(0.09)	<0.27	97.6(0.2)	5.5(0.4)
	−02 42 36	not observed							
G30.8-0.1	18 45 11.0	3.09(0.11)	2.44(0.10)	1.74(0.08)	1.63(0.08)	0.58(0.07)	0.21(0.07)	98.9(0.1)	7.0(0.0)
	−01 57 57	2.18(0.16)	1.36(0.15)	1.18(0.08)	1.10(0.09)	0.32(0.08)		99.0(0.2)	7.9(0.3)
G34.26+0.15	18 50 46.1	3.72(0.15)	2.97(0.15)	2.20(0.14)	2.41(0.14)	1.31(0.13)	0.65(0.1)	58.7(0.1)	6.0(0.1)
	01 11 12	2.22(0.13)	2.06(0.12)	1.29(0.09)	1.28(0.10)	0.61(0.09)		58.5(0.2)	6.9(0.2)
G35.19-0.74	18 55 40.8	0.75(0.06)	0.88(0.07)	0.36(0.06)	<0.18			33.7(0.2)	4.6(0.2)
	01 36 30	not observed							
W 48	18 59 13.8	0.32(0.08)[1]	0.15(0.07)[1]	<0.2				43.9(0.6)	4.2(0.6)
	01 09 20.0	not observed							
W 49N	19 07 49.9	1.71(0.89)	1.69(0.98)	0.81(0.32)	1.59(0.33)	< 0.93		9.4(1.6)	16.0(1.3)
	09 01 14	1.05(0.19)	0.90(0.15)	0.99(0.15)	1.16(0.15)	< 0.45		9.2(1.0)	19.8(1.1)
W 51E1/E2	19 21 26.2	4.89(0.16)	4.21(0.15)	3.34(0.10)	3.76(0.10)	1.87(0.10)	0.67(0.07)	56.8(0.1)	9.5(0.1)
	14 24 43	2.86(0.11)	2.13(0.11)	1.63(0.11)	1.87(0.08)	0.72(0.08)		57.3(0.1)	10.8(0.2)
W 51 MET3	19 21 27.5	0.65(0.14)	0.59(0.13)	0.50(0.10)	0.42(0.11)	<0.27		55.5(0.6)	8.0(0.7)
	14 23 52	not observed							
Onsala 1	20 08 09.9	0.56(0.05)	0.55(0.05)	0.24(0.05)	<0.12			11.9(0.2)	4.7(0.2)
	31 22 42	<0.18							
W 75N	20 36 50.0	not observed							
$(0'', 0'')$	42 26 58	not observed							
		0.75(0.03)	0.67(0.03)	0.46(0.03)	0.47(0.03)	0.34(0.03)	0.09(0.03)	9.1(0.1)	5.6(0.1)
W 75N	20 36 50.4	0.86(0.07)	0.84(0.07)	0.35(0.06)	0.36(0.06)	<0.18		9.4(0.2)	4.8(0.2)
$(6'', 25'')$	42 27 23	0.39(0.06)	0.30(0.06)	< 0.18				9.6(0.3)	4.8(0.5)
DR 21 West	20 37 07.8	0.19(0.06)[1]	0.16(0.08)[1]	< 0.21				−2.1(1.2)	5.0(0.0)
	42 08 44.0	not observed							
DR 21	20 37 13.0	0.61(0.09)	0.47(0.08)	0.16(0.08)	0.23(0.09)	< 0.21		−2.1(0.2)	2.7(0.0)
	42 08 50.0	0.63(0.05)	0.49(0.05)	0.20(0.05)	0.11(0.05)	< 0.15		−2.2(0.1)	3.7(0.2)
DR 21(OH)	20 37 13.8	1.53(0.06)	1.43(0.06)	0.74(0.05)	0.64(0.05)	<0.15		−3.1(0.1)	4.7(0.1)
	42 12 13	0.97(0.07)	1.03(0.07)	0.30(0.06)	0.25(0.06)	< 0.21		−3.0(0.2)	4.7(0.0)
L 1157	20 38 39.6	<0.09							
$(0'', 0'')$	67 51 33	not observed							
L 1157	20 38 41.0	0.23(0.05)	0.21(0.05)	<0.12				2.1(0.5)	4.9(0.6)
$(20'', -60'')$	67 50 33	not observed							
S 140	22 17 41.2	0.39(0.04)	0.30(0.04)	0.26(0.05)	<0.12			−6.8(0.1)	3.1(0.2)
	63 03 43	0.34(0.12)	0.14(0.09)	0.15(0.09)	< 0.36			−7.0(0.6)	3.8(1.1)
Cep A	22 54 19.2	0.30(0.04)	0.31(0.04)	0.08(0.03)	0.17(0.04)	<0.12		−9.9(0.2)	3.6(0.3)
	61 45 47	0.24(0.05)	0.22(0.05)	< 0.15				−10.3(0.4)	3.9(0.5)
NGC 7538	23 11 36.6	0.45(0.04)	0.42(0.04)	0.22(0.04)	0.25(0.04)	<0.12		−57.7(0.2)	4.0(0.2)
IRS1	61 11 50	0.25(0.05)	0.15(0.05)	< 0.12				−57.3(0.5)	4.0(0.0)
NGC 7538S	23 11 36.1	1.06(0.05)	0.84(0.05)	0.57(0.05)	0.34(0.04)	<0.12		−55.4(0.1)	4.5(0.1)
	61 10 30	0.74(0.09)	0.41(0.09)	0.22(0.08)	< 0.24			−55.6(0.4)	4.5(0.4)
		0.40(0.02)	0.33(0.02)	0.18(0.02)	0.16(0.02)	<0.05		−55.7(0.1)	5.1(0.2)

[1]–marginal detection

ratios between the $6_K - 5_K$ $CH_3^{13}CN/CH_3^{12}CN$ line intensities in G34.26+0.15 were found by Akeson & Carlstrom (1996).

In all the observed sources we detected the 1–0 ^{13}CO line. In addition, in several objects we found HNCO, $HCOOCH_3$, and the deuturated species NH_2D and CH_3OD. These data will be discussed elsewhere.

4. Rotational diagrams

The molecular gas properties were derived in two ways. First, the rotational diagram analysis, as described by Turner (1991) was carried out. The Boltzmann plots are shown in Fig. 5. Since the the sources are typically smaller than the beams and the beam filling factors at 110, 92, and 147 GHz are different, we analyzed different groups of lines separately. The same main features are present both in the 110 and 92 GHz rotational diagrams.

Fig. 5 shows that the majority of the plots cannot be fitted by straight lines. First, in some objects the points that correspond to the $K = 3$ levels are located much lower than the fitted lines. Examination of previous data (e.g. line intensities, published by Churchwell et al. 1992, or Olmi et al. 1993) in a number of sources shows the same

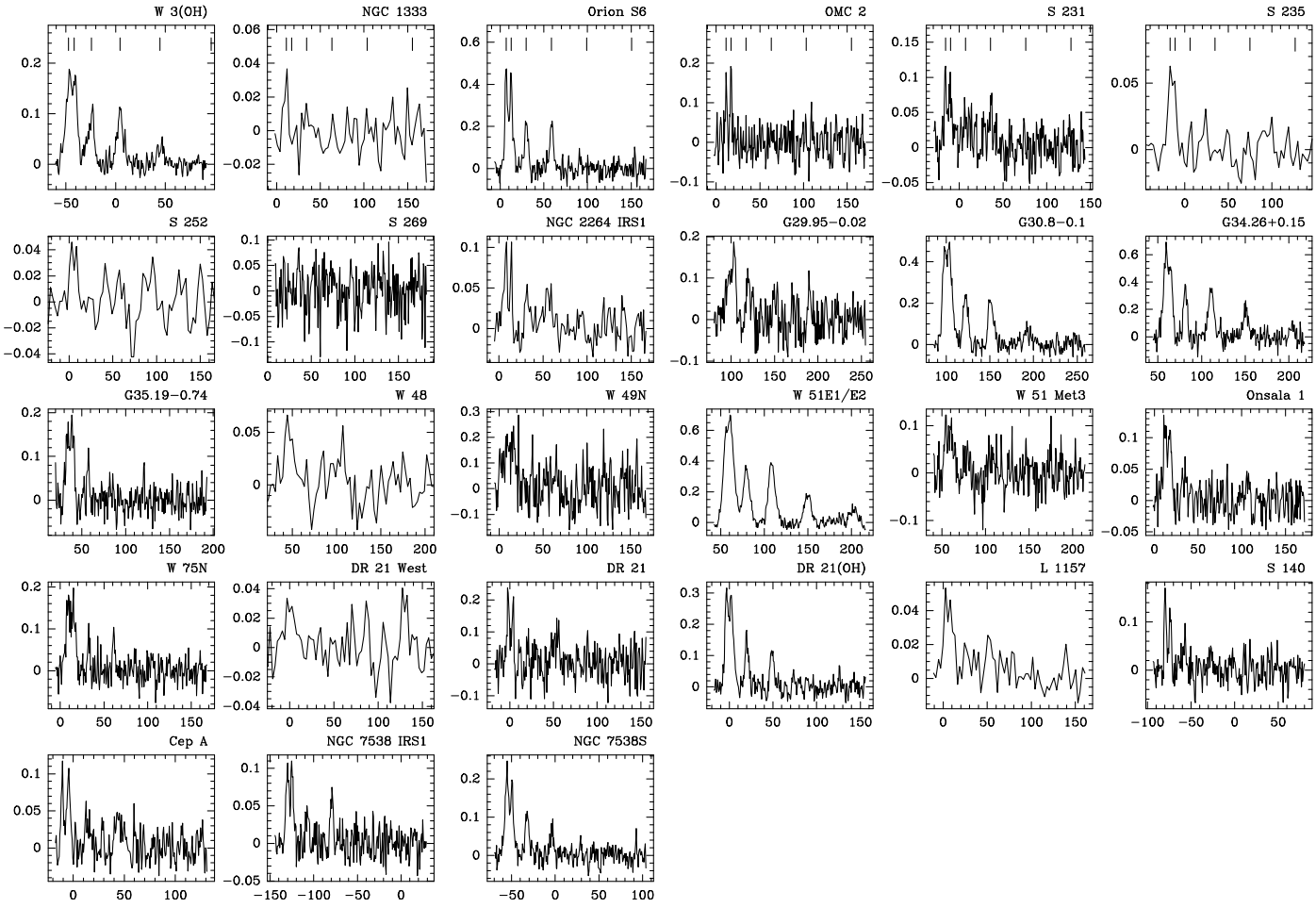

Figure 1: Spectra of the sources, observed at 110 GHz. x-axis: LSR velocity of the $6_0 - 5_0$ line in km s^{-1}; y-axis: antenna temperature in Kelvins. Vertical lines in the upper row indicate the positions of 0 to 5 K-components, K values increase to the right.

$K = 3$ decrease, which proved to be a rather common feature and should be explained. Symmetry requirements divide the CH_3CN molecule into two independent species, A and E, with the $K = 3n$ rotational levels belonging to the A species and the $K = 3n \pm 1$ levels belonging to the E species. The $K = 3$ levels belong to the A species suggesting that the A species may be underpopulated relative to E; but in this case the $K = 0$ levels should be underpopulated as well, in contradiction with Fig. 5.

Presumably the $K = 3$ decrease is caused by high optical depths. We constructed rotational diagrams following Turner (1991), i.e. we plotted $N_{\rm u}/g_{\rm u}$ (see Eq. 1) versus E_u/k. Here $g_{\rm u}$ is the upper level statistical weight, equal to the product of the rotational degeneracy $g_{\rm J} = (2J+1)$, the K-level degeneracy $g_{\rm K}$, and the reduced nuclear spin statistical weight $g_{\rm I}$. In symmetric tops the product $g_{\rm I}g_{\rm K}$ for the $K = 3n$, $n \neq 0$ levels is two times larger than that for the other levels (Turner 1991). The level populations for rotational diagrams are calculated assuming optically thin lines

$$\frac{N_{\rm u}}{g_{\rm u}} = \frac{3k \int T_{\rm br}\, dV}{8\pi^3\mu^2\nu S_{\rm ul} g_{\rm I} g_{\rm K}} \qquad (1)$$

Here μ is the permanent dipole moment, ν is the line frequency, $S_{\rm ul}$ is the line strengh, k is the Boltzmann constant and $T_{\rm br}$ is the brightness temperature. We used the main-beam brightness temperature $T_{\rm mb}$ instead of the unknown $T_{\rm br}$. Eq. 1 implies that $\int T_{\rm br}\, dV$ is proportional to optical depth. In the case of optically thick emission Eq. (1) underestimates $N_{\rm u}/g_{\rm u}$, the higher the optical depth (proportional to the statistical weight of the upper level), the stronger is the underestimate. So, the population of the more degenerate $K = 3$ levels is underestimated to a larger degree than the population of the adjacent levels.

The effect of optical depth is demonstrated in Fig. 5(D) where model rotational diagrams for three parameter sets are shown. One can see in the diagram for high density

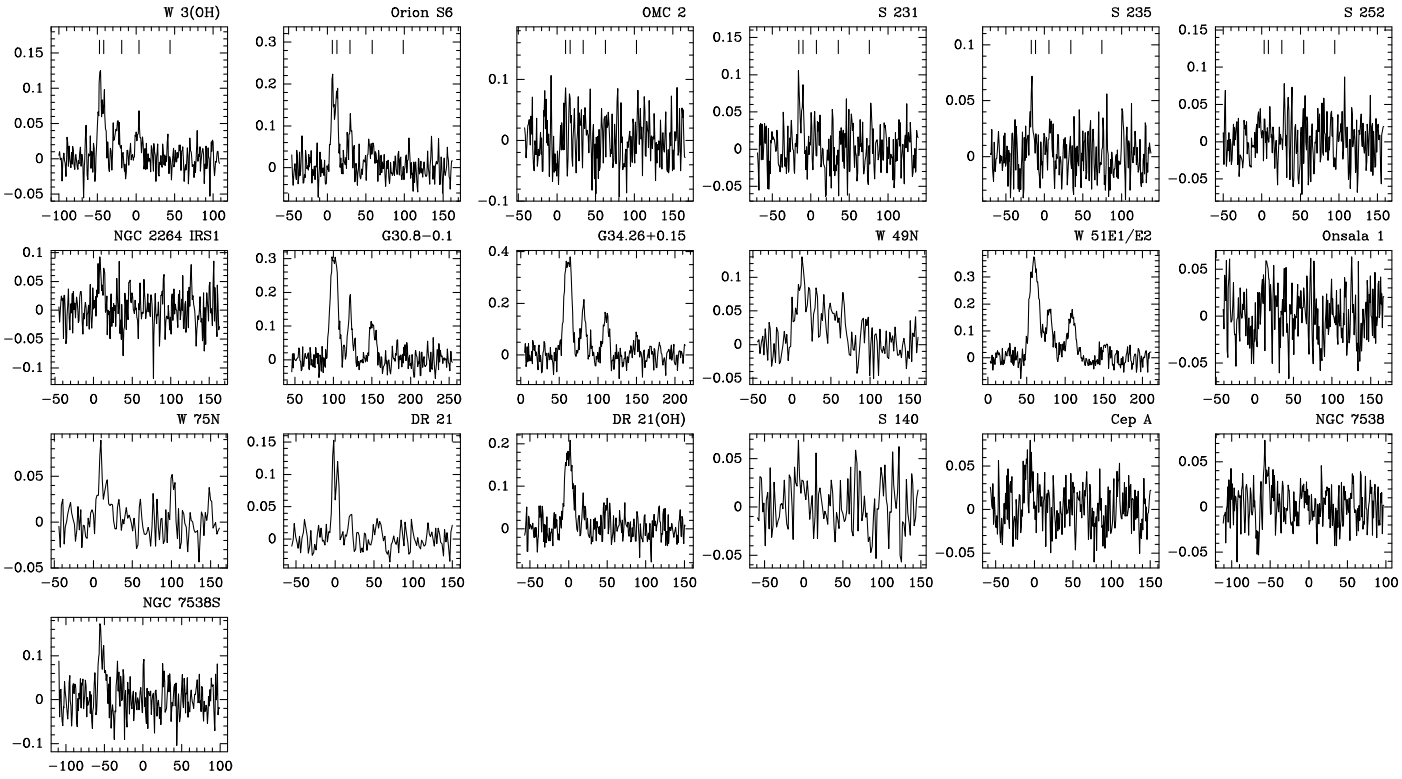

Figure 2: Spectra of the sources, observed at 92 GHz. x-axis: LSR velocity of the $5_0 - 4_0$ line in km s^{-1}; y-axis: antenna temperature in Kelvins. Vertical lines in the upper row indicate the positions of 0 to 4 K-components, K values increase to the right.

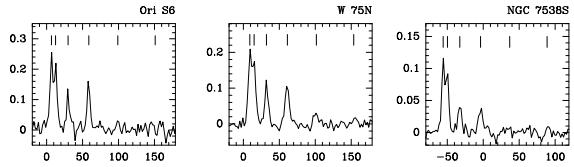

Figure 3: Spectra of the sources, observed at 147 GHz. x-axis: LSR velocity of the $8_0 - 7_0$ line in km s^{-1}; y-axis: antenna temperature in Kelvins. Vertical lines indicate the positions of 0 to 5 K-components, K values increase to the right.

and optically thick lines the same $K = 3$ decrease. Thus, the rotational diagrams, like the marginal detection of the $^{13}CH_3CN$ lines, suggest that the CH_3CN lines may be optically thick.

Fig. 5(D) shows that for a density of 3×10^3 cm^{-3} there is no $K = 3$ decrease even in the case of optically thick lines. For low density and optically thick emission the excitation of the $5_K - 4_K$ and $6_K - 5_K$ lines is determined by internal radiation rather than collisions. Larger optical depth of the $K = 3$ lines leads to higher excitation and brightness temperature of these transitions and to the absence of the $K = 3$ decrease. Examinaton of a large number of models showed that a significant $K = 3$ decrease appears if the density is of the order of 10^5 cm^{-3} or larger. Hence, the absence of the $K = 3$ decrease shows that either the lines are optically thin or the gas density is low.

Rotational temperature, derived from optically thick lines, is larger than gas kinetic temperature. For example, the rotational temperature for model 2 is 246 K and that for model 3 is 341 K versus the gas kinetic temperature 100 K.

The parameters, derived from the rotational diagrams are presented in Table 3. On the basis of the discussion above the sources were divided into two groups. The sources in group I are those that show significant $K = 3$ decrease. We can conclude that the 110 and 92 GHz lines are optically thick and that the gas density is about 10^5 cm^{-3} or larger. Since for optically thick $J_K - (J-1)_K$ CH_3CN lines rotational diagrams give exaggerated temperatures, the kinetic temperatures of group I sources in Table 3 are upper limits. On the other hand, high optical depth, as well as beam dilution (note, that both ME images and indirect size estimates in Table 4 demonstrate that the group I sources are very compact), leads to an underestimation of column density. Hence, the column densities of group I sources in Table 3 are lower limits. The sources in group II are those where the $K = 3$ decrease is either absent or cannot be found since the $K = 4$ lines, adjacent to the $K = 3$ lines, are not detected. The

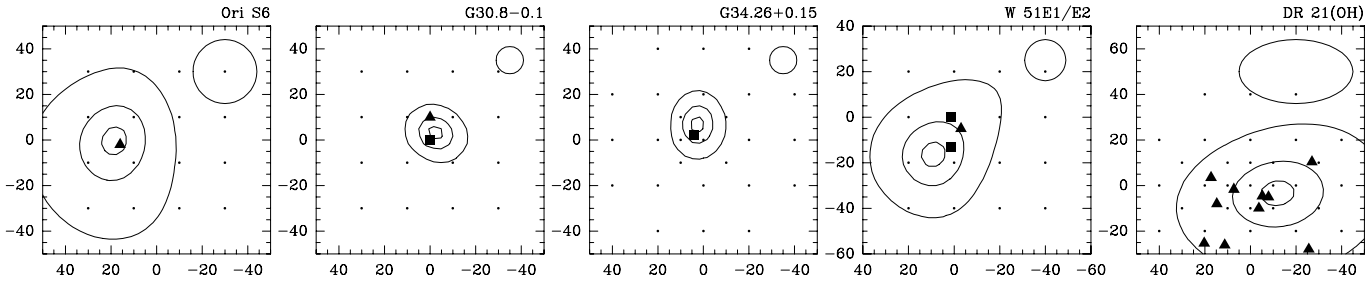

Figure 4: Maximum entropy maps of five sources. x and y axes are R.A. and DEC. offsets (arcsec), respectively, from the (0,0) positions, given in Table 2. The observed positions are marked by dots. The contours correspond to 10, 50 and 90% of the deconvolved integrated intensity peak values, which are 21.9 K km s^{-1} for Ori S6, 57.7 K km s^{-1} for G30.8-0.1, 77.6 K km s^{-1} for G34.26+0.15, 25.6 K km s^{-1} for W 51E1/E2, and 7.3 K km s^{-1} for DR 21(OH). The effective HPBW of the reconstruction are represented by ellipses in the upper right corners. For DR 21(OH) the resolutions in the two coordinates are different due to the cosine effect. Filled squares show H_2O maser positions, filled triangles show the positions of thermal methanol peaks, taken from Menten et al. 1988 (Ori S6), Liechti & Wilson 1996 (G30.8-0.1, G34.26+0.15, W 51E1/E2); Liechti & Walmsley 1997 (DR 21(OH)).

Table 3: Parameters derived from the rotational diagram analysis. Columns: 1, source name; 2, group (see text for definition); 3, rotational temperatures derived from the 110 GHz lines; 4, rotational temperatures derived from the 92 GHz lines; 5, CH_3CN column densities derived from the 110 GHz lines.

Source	Group	$T_{\rm rot}$ (K)			$N_{\rm CH_3CN}$
		(110)	(92)	(147)	(10^{12}cm^{-2})
W 3(OH)	I[1]	120	63		
Ori S6	II	46	46	62	33
S 231	II	80			9
NGC 2264	II	43			7
G29.95-0.02	I	1013			
G30.8-0.1	I	125	142		
G34.26+0.15	I	418	295		
G35.19-0.74	II	40			11
W 49N	II	117			76
W 51E1/E2	I	265	349		
W 51 Met3	II	77			18
Onsala 1	II	36			7
W 75N(0″, 0″)	II			78	
W 75N(6″, 25″)	II	47			13
DR 21	II	23	32		5
DR 21(OH)	II	48	36		24
S 140	II	42			18
Cep A	II	57			5
NGC 7538	II	62			9
NGC 7538S	II	42	30	44	15

[1] W 3(OH) is referred to the group I since the $K = 3$ decrease is present at 110 GHz and the nature of this source (hot core) is similar to that of other group I sources (see below).

reliability of the rotational temperatures and column densities of the group II sources is discussed in section 7.

In G34.26+0.15, and, probably, G30.8-0.1 and W 51E1/E2 the low excitation $K = 0$ and $K = 1$ levels have excess population. The same effect can be noticed in the model rotational diagram for low density [Fig. 5(C)]. However, the excess population is present in the rotational diagrams of group I sources, which we believe to be dense. Therefore this excess indicates their complex structure. For simplicity we call them core–halo objects. Here "halo" means any colder or less dense source(s) than "core". Core-halo structure of CH_3CN emission has been already detected in several objects (Olmi et al. 1996).

5. Statistical equilibrium calculations

To determine source properties by means of statistical equilibrium (SE) calculations, we used the approach, similar to that applied to CH_3CN analysis, e.g. by Bergman & Hjalmarson (1989) and Olmi et al. (1993). The LVG code was kindly made available by C.M. Walmsley and R. Cesaroni. The free parameters of the model are the gas kinetic temperature $T_{\rm kin}$, the molecular hydrogen number density $n_{\rm H_2}$, and the methyl cyanide density, divided by velocity gradient $n_{\rm CH_3CN}/(dV/dR)$.

To obtain SE parameters, one should perform SE calculations for a number of parameter sets and choose the sets which are in agreement with observational data. The agreement between our observations and SE models can be evaluated by comparing model line intensity ratios within the 110, 92, and 147 GHz series with the corresponding observed ratios. For each line series we used the ratios $R_{\rm i} = T_{\rm mb}(J_K - (J-1)_K)/T_{\rm mb}(J_2 - (J-1)_2)$.

We modelled the CH_3CN brightness temperatures for the kinetic temperatures 10–500 K, the molecular hydro-

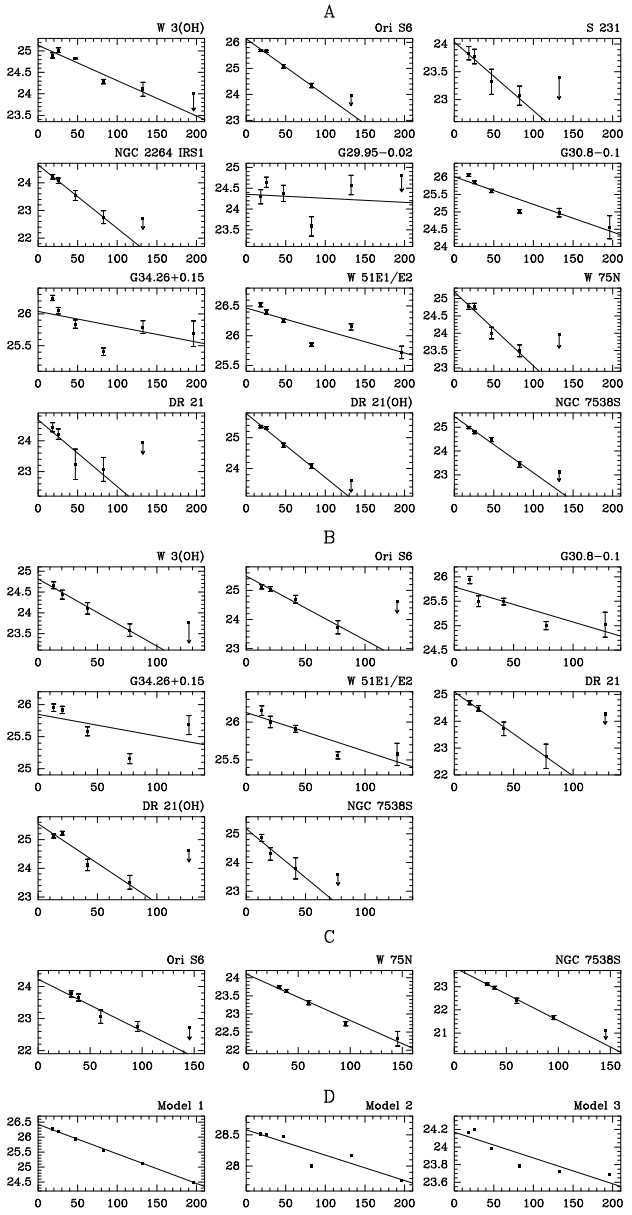

Figure 5: Rotational diagrams: $\ln(N_u/g_u)$ versus E_u/k (K). Arrows denote upper limits at 3σ level. **A,** 110 GHz; **B,** 92 GHz; **C,** 147 GHz; **D,** model rotational diagrams for the 110 GHz lines. The model parameters are as follows: Model 1, n_{H_2}=10^6 cm^{-3}, $T_{\rm kin}$ = 100 K, optical depth of the 6_3-5_3 line $\tau_3 = 0.1$; Model 2, n_{H_2}=10^6 cm^{-3}, $T_{\rm kin}$ = 100 K, τ_3 = 1.8; Model 3, n_{H_2}=$3\times\ 10^3$ cm^{-3}, $T_{\rm kin}$ = 100 K, $\tau_3 = 3.5$.

gen number densities 3×10^3–10^8 cm^{-3}, and the CH_3CN densities, divided by a velocity gradient in the range 10^{-7}–10 cm^{-3}/(km s^{-1} pc^{-1}). External radiation, except the microwave background, was neglected. The best-fit models are those that minimize the χ^2 value

$$\chi^2 = \sum_i \left(\frac{R_{\rm i}^{\rm obs} - R_{\rm i}^{\rm mod}}{\sigma_{\rm i}^{\rm obs}} \right)^2 \qquad (2)$$

where $\sigma_{\rm i}^{\rm obs}$ are the rms errors of the observed ratios. We calculated χ^2 for all models and then found the minimum values. The 1σ confidence levels were calculated as described in Lampton et al. (1976).

For G30.8-0.1, G34.26+0.15 and W 51E1/E2 the minimum χ^2 values are much larger than expected from the number of degrees of freedom. This fact confirms our suggestion that these sources cannot be described within the frames of a homogeneous source model. Bearing in mind our assumption about their core–halo structure and arbitrarily suggesting that the core contribution dominates in the $K \geq 2$ emission, we determined the core parameters using only the $K \geq 2$ lines (core parameters below). This procedure virtually did not change temperatures derived from all the observed lines. For 34.26+0.15 an interferometric hot core spectrum at 110 GHz (Akeson & Carlstrom, 1996) is well approximated by our core models, showing that this approach is reasonable.

Finally, for each model, appropriate for a given source, we estimated the source size $\theta_{\rm s}$, assuming a Gaussian brightness distribution

$$\frac{\theta_{\rm s}^2}{\theta_{\rm s}^2 + \theta_{\rm mb}^2} = \frac{T_{\rm mb}}{T_{\rm mod}} \qquad (3)$$

where $T_{\rm mod}$ is the model brightness temperature and $\theta_{\rm mb}$ is the FWHP. Using published distances, we estimated source linear sizes D, averaged velocity gradients $\Delta V/D$ and CH_3CN abundance

$$X_{\rm CH_3CN} = n_{\rm m}\ \Delta V/(D\ n_{H_2}) \qquad (4)$$

where $n_{\rm m}$ is the model $n_{\rm CH_3CN}/(dV/dR)$ value.

Like previous workers in the field, we found that only the kinetic temperature can be determined accurately enough by this method. For most sources, especially those of the group II, we could not obtain any density and hence, CH_3CN abundance estimate. To constrain these parameters, we left for further analysis only those models that agree with the observed ratios between the 110, 92 and 147 GHz line intensities, assuming that the observed intensities are accurate within 20%.

Our SE calculations confirm that the $K = 3$ decrease in the rotational diagrams appears as a result of line opacities. For the sources, which were considered optically thick due to the $K = 3$ decrease we found that only optically thick models correspond to the observational data. Model gas temperatures appeared lower than rotational temperatures for the same sources, as it is expected for optically thick lines. For other objects, the kinetic temperatures proved to be close to the rotational temperatures, and either only optically thin or both moderately optically thick and optically thin models satisfy the observational data.

The results of the SE analysis are presented in Table 4. For group I objects the SE modelling shows that only very compact sources satisfy the observed line intensity ratios. This conclusion is supported by the maximum entropy maps.

Table 4: Properties of the sources obtained from SE calculations. Columns: 1, source name; 2, kinetic temperature; 3, CH_3CN abundance; 4, adopted distance; 5, angular diameter; 6, density.

Source	$T_{\rm kin}$ (K)	$X_{\rm CH_3CN}$ ($\times 10^{-10}$)	d (kpc)	θ ($''$)	$n_{\rm H_2}$ (10^4cm^{-3})
W 3(OH)	70(50–95)	10–1000	2.2	2-4[b]	$\geq$10
Ori S6	45(40–50)	0.3–30	0.5	≥ 10	10–100
S 231	55(35–160)		2	≥ 3	
NGC 2264	45(25–65)		0.8	≥ 3	
G30.8-0.1[a]	60(45–75)	≥ 100	8	2-7	
G34.26+0.15[a]	140(65–220)	≥ 300	3.8	1-6[c]	
W 51E1/E2[a]	160(120–180)	100–1000	8	1-3	≥ 30
W 75N($6'', 25''$)	40(35–60)		3	≥ 5	≥ 1
DR 21	30(20–55)		3	≥ 5	
DR 21(OH)	45(40–55)	1–100	3	≥ 8	≥ 3
NGC 7538	50(35–100)		3.5	≥ 3	
NGC 7538S	40(30–45)	10–100	3.5	5-9	10–100

[a]–core parameters
[b]–less than $1''$ according to Wink et al. (1994).
[c]–$3.9'' \times 3.3''$ (Akeson & Carlstrom, 1996).

6. Comments on selected sources

W 3(OH). Wink et al. (1994) published a map of this source in the $5_3 - 4_3$ CH_3CN line, obtained with the Plateau de Bure interferometer and found two compact objects, a strong clump located toward the water maser cluster and HCN peak, known as TW object (Turner & Welch, 1984), and a much weaker one toward the UC HII region. Our temperature estimate is in a good agreement with that of Wink et al.; however, we found that source size is larger than $2''$, in conflict with their upper limit of $1''$ for the stronger clump. For the core models the lower limit appeared to be less than $1''$. We suggest that our single-dish CH_3CN line ratios are affected by the contribution from the weaker clump and by a possible halo emission, which is too weak or too extended to be found with the Plateau de Bure interferometer.

G34.26+0.15. An interferometer map of this well-known hot core (Ohishi 1996) in the $6_K - 5_K$ CH_3CN lines have been already obtained by Akeson & Carlstrom (1996). The ratios of all the observed by us line intensities toward this source could not be fitted by homogeneous source models, suggesting a core–halo structure. The core model, which is in the best agreement with our data, fairly well represents the interferometric spectrum by Akeson & Carlstrom. The core temperature appeared to be about 140 K, although with large uncertainity. This value is much lower than the 250 K obtained by Akeson & Carlstrom; the discrepancy is probably appeared due to different accounts of optical depth effects. We could not obtain any density estimate from our data only; however, the brightness temperature, which can be obtained using the source size by Akeson & Carlstrom (1996) requires a density larger than 10^5 cm^{-3}.

W 51E1/E2. The CH_3CN source was found toward the radio continuum objects E1 and E2, which are associated with the H_2O and OH masers W 51 Main/South, ammonia peaks NH_3-1 and NH_3-2, detected at VLA (Ho et al. 1983), and emission of other molecules, typical for hot cores (Ohishi 1996). The peak of the CH_3CN emission is coincident within the pointing error of $5''$ with the ammonia clump NH_3-1; however, the peak position accuracy is not good enough since the peak is close to the edge of the mapped region. Without further observations we cannot state that the CH_3CN peak is coincident with any of the mentioned objects. There is a weak tongue towards the peak of thermal methanol emission (Liechti & Wilson 1996), suggesting that the structure of the CH_3CN source is complex. The observed lines cannot be fitted within the frames of the model of a homogeneous source. The core models give a kinetic temperature of about 160 K, density larger than 3×10^5 cm^{-3}, and core diameter between $1''$ and $3''$.

DR 21(OH). The peak of the CH_3CN brightness coincides with the methanol maser and peak of thermal emission DR 21(OH)-2 (Liechti & Walmsley 1997). We could not find a homogeneous source model that fits the observed data well enough ($\chi^2_{\rm min} = 8.4$ instead of expected value of 3), suggesting that the structure is complex, as it was already found for methanol and other molecules (Liechti & Walmsley 1997 and references therein). However, the non-detection of the lines with $K > 3$ precludes core–halo analysis.

7. Discussion

SE analysis shows that the group I sources are very different from the others. These are the strongest sources in our sample and have kinetic temperatures higher than the group II sources. All of them, except G30.8-0.1, are well-known hot cores (Wink et al. 1984; Ohishi 1996).

The CH_3CN abundance in these objects is about or larger than 10^{-9} and larger than in the group II objects. The CH_3CN abundance of order of 10^{-8} have been reported toward hot cores, e.g. in Orion (Blake et al. 1987) and in G10.47+0.03 (Olmi et al. 1993). Presently, the fact that the CH_3CN abundance in hot cores is increased due to evaporation of molecular material from icy mantles of interstellar grains is well established. CH_3CN may be either a parent molecule or may be a product of a chain of gas-phase reactions, starting from HCN or some other nitrogen-bearing molecule, which appears in gas phase due to mantle evaporation (see e.g., Millar 1996 and references therein). This scenario is in agreement with the current observational data on hot cores and has further support in the results of the observations of comets. Both HCN and CH_3CN , as well as some other nitrogen-bearing species, were identified as parent molecules in cometary comae (Bockelée-Morvan 1996; Biver et al. 1998). Since cometary ices may consist of interstellar material, this is an indication that grain mantle evaporation can be a source of CH_3CN .

Most hot cores, observed in CH_3CN lines, are sites of massive star formation. Other regions, where gas-phase chemistry is strongly affected by grain mantle evaporation, are bow shocks at the edges of y oung bipolar outflows, driven by low-to-intermediate mass protostars (Bachiller 1996). The temperature in these objects is high enough to evaporate grain mantles, and ammonia and HCN abundance is strongly enhanced here, as well as the contents of some other molecules, abundant in hot cores. Thus, one can expect high CH_3CN abundance in these regions. We observed two such objects, NGC 1333 IRAS2 and L 1157. In L 1157, no lines were found toward the central source ($0'', 0''$ position), but a weak emission was detected toward the blue wing of the outflow ($20'', -60''$ position), where the abundance of HCN, NH_3, CH_3OH and some other molecules is enhanced up to several orders of magnitude (Bachiller & Pérez Gutiérrez 1997, and references therein). We estimated the CH_3CN abundance assuming that the CH_3CN emission arise in the same small region as the NH_3 emission (B1 in the notation of Tafalla & Bachiller 1995). Assuming B1 size about $10''$–$15''$ and kinetic temperature 80 K (Tafalla & Bachiller 1995) we obtained the CH_3CN column density of about 2×10^{13} cm^{-2}. H_2 column density of 2.4×10^{21} cm^{-2} follows from the ^{18}CO data by Bachiller & Pérez Gutiérrez (1997). Hence, CH_3CN abundance is about 10^{-8}, as high as in hot cores. Thus, our data show that CH_3CN may be enhanced toward the blue wing of this bipolar outflow. Sensitive high-resolution observations are desirable to check this conclusion.

We did not detect any emission toward the red wing of the NGC 1333 IRAS2 E–W outflow, where CS and CH_3OH enhancement has been found by Sandell et al. (1994), except a weak spike at about 2.5 σ level, which can be attributed to the $6_0 - 5_0$ line. The CS column density at this position, derived by Langer et al. (1996), is an order of magnitude lower than the CS column density toward L 1157 B1, presented by Bachiller & Pérez Gutiérrez (1997), showing that either gas column density or molecular enhancement or both are smaller in NGC 1333 IRAS2 E–W, leading to the non-detection of the CH_3CN emission.

The nature of the group II sources is unclear. On the one hand, their rotational diagrams do not demonstrate significant point deviations from the fitted lines. Therefore the conditions, necessary for the application of rotational diagrams may be fulfilled, in particular, the sources may be uniform and the observed lines may be optically thin. In this case, these objects are warm clouds (50 K or lower). On the other hand, the good appearance of rotational diagrams does not *prove* that these conditions are fulfilled. The sources may be inhomogeneous or/and the lines may be optically thick. In particular, since the intensities of the $K = 4$ lines are unknown, we cannot distinguish between an opaque core–halo source or an optically thin uniform cloud, colder than the core. This statement can be explained as follows. Let us consider a rotational diagram of an optically thick core–halo object. A high optical depth leads to an apparent decrease of the N_3/g_3 value and to the $K = 3$ decrease, while the halo contribution leads to an increase of the N_0/g_0 and N_1/g_1 values. Therefore the slope of the fitted line, drawn over the $K = 0$–3 points, is larger than the slope that corresponds to the core, and provides a lower temperature. Since signal-to-noise ratios are typically rather poor in our spectra of group II sources, neither rotational diagrams nor χ^2 analysis make it possible to distinguish between the two source models. Therefore it is possible that at least some of the group II objects are the same as those of group I, i.e. consist of compact opaque hot cores and colder halos. Note, that the presence of hot gas in most of the observed group II sources is indicated by e.g. water vapor maser emission. Therefore more sensitive observations are required to study the structure of these objects. Below we assume that the group II sources are homogeneous; all the results, obtained from the rotational diagrams and SE analysis are valid only if this assumption is correct.

The temperatures of the group II sources proved to be about 50 K or lower and the CH_3CN abundance proved to be either below $\approx 10^{-9}$ or cannot be estimated from our data. We have no size estimates for these sources, apart from very uncertain lower limits. Density estimates, where available, show that it is at least larger than 10^4 cm^{-3}. One can suggest that the CH_3CN emission arise in warm clouds, well-known from the observations of CS, NH_3 and other molecules. One of the best studied warm clouds is NGC 2264 IRS1. Our temperature estimate from Table 4 agrees with the value of 55 K, obtained by Schreyer et al. 1997 on the basis of a careful study of this source in a large number of lines of different molecules. Thus, the assumption that the CH_3CN emission in the group II sources arise in warm (30–50 K), dense (10^4 cm^{-3} or larger) gas may be correct, but to date we cannot exclude the possibility that at least in some of these sources the emission from hot and compact objects with enhanced CH_3CN abundance may be present (see the previous paragraph).

8. Summary and conclusions

A survey of 27 galactic star-forming regions in the 6_K-5_K, 5_K-4_K, and 8_K-7_K CH_3CN lines at 110, 92, and 147 GHz, respectively, was carried out. Twenty-five sources were detected at 110 GHz, nineteen at 92 GHz and three at 147 GHz.

A number of source parameters were derived using rotational diagram analysis and statistical equilibrium calculations. As expected, the strongest CH_3CN emission was found towards hot cores. The kinetic temperatures of these sources are of the order of or larger than 100 K, the CH_3CN abundances are larger than 10^{-9}, and the lines are optically thick. Hot cores are usually associated with colder/less dense gas. Probably, the CH_3CN abundance in the hot gas, associated with the young bipolar outflow L 1157, is about 10^{-8}.

The nature of weaker objects is unclear. CH_3CN emission may arise in warm (30–50 K) dense ($> 10^4$ cm^{-3}) clouds. However, at least in some of these sources hot compact objects with enhanced CH_3CN abundance may be present.

Acknowledgements The authors are grateful to the staff of the Onsala Space Observatory for providing help during the observations. We are grateful to Dr. S. Radford (NRAO) for scheduling the 147 GHz observations and the staff of 12-m NRAO telescope for the help during the observations. We would like to thank Dr. V.I. Slysh for helpful discussions and Drs. C.M. Walmsley and R. Cesaroni for making available the LVG code. The work was done under partial financial support of the Russian Foundation for Basic Research (grant No 95-02-05826) and the project *N*315 "Radio Astronomy Educational and Scientific Center" within the frames of the program "State Support for the Integration of High School and Basic Research". Onsala Space Observatory is the Swedish National Facility for Radio Astronomy and is operated by Chalmers University of Technology, Göteborg, Sweden, with financial support from the Swedish Natural Science Research Council and the Swedish Board for Technical Development.

References

Akeson R.L., Carlstrom J.E., 1996, ApJ 470, 528

Bachiller R., 1996, Observations of shocks and outflows, in: Molecules in Astrophysics: Probes and Processes, ed. E.F. van Dishoeck, Kluwer Academic Publishers, Dordrecht, p. 103

Bachiller R., Pérez Gutiérrez M., 1997, ApJ 487, L93

Bergman P., Hjalmarson Å., 1989, Methyl cyanide (CH_3CN) in molecular cloud cores, in: The Physics and Chemistry of Interstellar Molecular Clouds, eds. G. Winnewisser, J.T. Armstrong J.T., Springer-Verlag, Berlin, p. 124

Biver N., Winnberg A., Bockelée-Morvan D., Colom P., Crovisier J., Gerard E., Germain B., Lellouch E., Moreno R., Davies J.K., Dent W.R.F., Paubert G., Wink J., Despois D., Lis D.C., Mehringer D., Benford D., Gardner M., Phillips T.G., Gunnarsson M., Rickman H., Bergman P., Johansson L.E.B., Rauer H., 1998, DPS meeting 30.5519

Blake G.A., Sutton E.C., Masson C.R., Phillips T.G., 1987, ApJ 315, 621

Bockelée-Morvan D., 1996, Cometary volatiles, in: Molecules in Astrophysics: Probes and Processes, ed. E.F. van Dishoeck, Kluwer Academic Publishers, Dordrecht, p. 219

Boucher D., Burie J., Bauer A., Dubrulle A., Demaison J., 1980, J. Phys. Chem. Ref. Data 9, 659

Cezaroni R., Walmsley C.M., Churchwell E., 1992, A&A 256, 618

Cezaroni R., Churchwell E., Hofner P., Walmsley C.M., Kurtz S. 1994, A&A 288, 903

Churchwell E, Walmsley C.M., Wood D.O.S., 1992, A&A 253, 541

Güsten R., Ungerechts H., 1985, A&A 145, 241

Ho P.T.P., Genzel R., Das A., 1983, ApJ 266, 596

Hollis J.M., Snyder L.E., Blake D.H., Lovas F.J., Suenram R.D., Ulich B.L., 1981, ApJ 251, 541

Irvine W.M., Goldsmith P.F., Hjalmarson Å, 1987, in: Interstellar Processes, eds. D.J. Hollenbach, H.A.Thronson Jr. Reidel, Dordrecht, p. 561

Kalenskii S.V., Dzura A.M., Booth R.S., Winnberg A., Alakoz A.V., 1997, A&A 321, 311

Lampton M., Margon B., Bowyer S., 1976, ApJ 208, 177

Langer W.D., Castets A., Lefloch B., 1996, ApJ 471, L111

Liechti S., Wilson T.L., 1996, A&A 314, 615

Liechti S., Walmsley C.M., 1997, A&A 321, 625

Loren R.B., Mundy L.G. 1984, ApJ 286, 232

Mauersberger R., Henkel C., Wilson T.L., Walmsley C.M. 1986, A&A 162, 199

Menten K.M., Walmsley C.M., Henkel C., Wilson T.L., 1988, A&A 198, 253

Millar T.J., 1996, Models of hot molecular cores, in: Molecules in Astrophysics: Probes and Processes, ed. E.F. van Dishoeck, Kluwer Academic Publishers, Dordrecht, p. 75

Moriarty-Schieven G.H., Snell R.L., Strom S.E., Schloerb F.P., Strom K.M., 1987, ApJ 319, 742

Ohishi M., 1996, Observations of hot cores, in: Molecules in Astrophysics: Probes and Processes, ed. E.F. van Dishoeck, Kluwer Academic Publishers, Dordrecht, p. 61

Olmi L., Cesaroni R., Walmsley C.M., 1993, A&A 276, 489

Olmi L., Cesaroni R., Neri R., Walmsley C.M., 1996, A&A 315, 565

Promislov V.G., 1999, Maximum entropy image restoration by evolutionary algorithm, in: Advances in Soft Computing - Engineering Design and Manufacturing, eds. R. Roy, T. Furuhashi, P.K. Chawdhry, Springer–Verlag, London, 421

Sandell G., Knee L.B.G., Aspin C., Robson I.E., Russell A.P.G., 1994, A&A 285, L1

Schreyer K., Helmich F.P., van Dishoeck E.F., Henning Th., 1997, A&A 326, 347

Slysh V.I., Kalenskii S.V., Val'tts I.E., Golubev V.V., Mead K., 1999, ApJS 123, 515

Solomon P.M., Jefferts K.B., Penzias A.A., Wilson R.W., 1971, ApJ 168, L107

Tafalla M., Bachiller R., 1995, ApJ 443, L37

Turner B.E., 1991, ApJS 76, 617

Turner B.E., Welch W.J., 1984, ApJ 287, L81

Wilczek R., Drapatz S., 1985, A&A 142, 9

Wink J.E., Duvert J., Guilloteau S., Güsten R., Walmsley C.M., Wilson T.L., 1994, A&A 281, 505

Wouterloot J.G.A., Walmsley C.M., Henkel C., 1988, A&A 203, 367